RSC Advances

PAPER

View Article Online
View Journal | View Issue

Check for updates

Cite this: *RSC Adv.*, 2025, **15**, 4236

A new quinoline-based fluorescent-colorimetric chemosensor for sensitive and selective "on–off" detection of Pb^{2+} ions†

Vanshika Sharma,[a] Srishti Dutta,[a] Devanand Sahu,[a] Abhilash Pandey,[a] Dishen Kumar,[a] Sanchita Das[b] and Goutam Kumar Patra *[a]

Received 18th November 2024
Accepted 21st January 2025

DOI: 10.1039/d4ra08193e

rsc.li/rsc-advances

For the first time, a novel mono Schiff base of a quinoline-based reversible fluorescent-colorimetric receptor (**L**) has been designed for the detection of Pb^{2+} ions in a semi-aqueous medium. The receptor **L** exhibited a very good selective fluorescent-colorimetric quick on–off response when exposed to Pb^{2+}. The colorimetric assay showed a sensitivity of 1.2×10^{-6} M, while the fluorescent assay exhibited a sensitivity of 9.9×10^{-7} M for Pb^{2+}. A 1 : 1 stoichiometric complexation between **L** and Pb^{2+} was determined using ESI-MS spectra and Job's plot measurements. Pb^{2+} was successfully measured using receptor **L** in both real samples and in an aqueous solution of the protein bovine serum albumin, as well as in the construction of an INHIBIT-type molecular logic gate.

1 Introduction

The environment has been contaminated by both living and non-living things, including hazardous bacteria, sewage discharge, animal waste, heavy metals, and industrial and municipal waste.[1] Heavy metal pollution has emerged as a major global environmental hazard as a result of the recent acceleration of industrialisation and growth. Lead (Pb^{2+}), mercury (Hg^{2+}), arsenic (As^{3+}), copper (Cu^{2+}), nickel (Ni^{2+}), cobalt (Co^{2+}), cadmium (Cd^{2+}), and chromium (Cr^{3+}) are examples of heavy metals that are frequently identified by their high levels of toxicity, long environmental half-lives, low levels of degradability, and water solubility. When certain hazardous metals are consumed or exposed to concentrations higher than permissible limits, human health may be adversely affected.[2]

Specifically, the widespread usage of lead ions (Pb^{2+}) has caused significant environmental harm and poses a danger to both human health as well as natural systems. The most frequent man-made sources of lead pollution in environmental matrices (water, soil, air, and food) include gasoline, paints, pigments, lead batteries, alloys, ceramics, glass, chemicals, toys, electronics, water pipes, solders, and other consumer goods.[3–6] Numerous natural processes, including weathering, mining, water sedimentation, and emissions from sea spray, can potentially release lead into the environment. Industrial workers engaged in mining, smelting, fitting, welding, manufacturing, construction, plumbing, jewellery making, refining, and other processes are more vulnerable to occupational exposure of lead.[7–10]

Excessive lead exposure has negative effects on the neurological, gastrointestinal, haematological, cardiovascular, reproductive, and renal systems in humans, leading to a variety of illnesses.[11–14] Although the enzyme machinery involved in metabolism and bodily repair remains unaffected, lead toxicity is notable for its effects on cellular components, such as cell membranes,[15] the endoplasmic reticulum,[16] and mitochondria.[17] Genomic instability, which includes genotoxicity, DNA damage, cell apoptosis, cell cycle arrest, and disruption of signal transduction pathways, can also result from prolonged exposure to lead.[18–21] Due to this exposure, children are more vulnerable to intellectual difficulties. Lead toxicity is a contemporary issue that affects human nutrition, evolution, and the environment.[22–24]

The WHO's lead regulations set the permissible lead intake limits at 0.01 mg L^{-1} in drinkable water and 0.2 μg m^{-3} in the air. A joint expert committee on food additives (JECFA) determined an acceptable consumption threshold of lead as 3.5 g per kg per body weight per day (WHO 2011b) to assist in preventing lead intake into the body.[25,26] However, even very low amounts of lead may be hazardous to health, especially in young children, therefore, there are no defined tolerable blood lead levels. Since lead does not participate in any biological processes in humans, it can be consumed or inhaled into the body, where it can be absorbed and attached to red blood cells.[27]

The need for the development of extraordinarily sensitive lead detection equipment has increased due to the pervasive pollution of lead and its deadly effects, even at low levels of exposure. Lead detection methods frequently make use of

---

[a] *Department of Chemistry, Guru Ghasidas Vishwavidyalaya, Bilaspur, C.G, India. E-mail: patra29in@yahoo.co.in; goutam.patra@ggu.ac.in; Tel: +91 7587312992*

[b] *Department of Chemistry, National Institute of Technology, Rourkela, Odisha, India*

† Electronic supplementary information (ESI) available: Fig. S1–S11, Tables S1 and S2 of this article can be found online. CCDC 2294084. For ESI and crystallographic data in CIF or other electronic format see DOI: **https://doi.org/10.1039/d4ra08193e**

electrochemical techniques such as atomic absorption spectroscopy (AAS),[28] atomic emission spectroscopy (AES),[29] capillary electrophoresis (CE),[30] X-ray fluorescence spectroscopy (XFS),[31] inductively coupled plasma-mass spectroscopy (ICP-MS),[32] and voltammetry.[33] It is very challenging to apply for field applications and laboratory analysis. Despite their exceptional sensitivity and selectivity, the majority of these analytical techniques have a number of drawbacks, including bulky and costly instrumentation, high running costs, challenges with on-the-spot detection, labour-intensive sample preparation procedures, and specialised maintenance. Using greater sample volumes, longer analytical periods, and sample pretreatment/preprocessing procedures are required for flame AAS-based lead detection. Comparably, ICP-MS-based detection necessitates highly qualified staff as well as expensive equipment and operating expenses. The narrow detection range, low specificity, and low accuracy of the electrochemical lead detection method based on anodic stripping voltammetry (ASV) have further limitations.[34] To fulfil the demand for highly selective, sensitive, quick, field-applicable, and miniaturized Pb^{2+} detection methods in a variety of media, the potential based on fluorescence, colorimetry, SPR, and SERS was investigated using a number of optical methodologies.[35,36] Due to its numerous benefits, the fluorescence detection method (high sensitivity, superior accuracy, and decreased detection limits) stands out among them as a reasonably straightforward and useful option. Additionally, on-site analyte detection is made possible by portable fluorescence-based sensors.

Lead shows strong coordination with ligands containing either soft or hard bases, such as sites for oxygen and nitrogen, because it is situated on the soft-hardness boundary. Schiff bases may therefore be the ideal coordinating sphere for lead ion detection. Because of their imine linkages, Schiff bases are a useful and significant class of electroactive chemicals that can form stable complexes with transition metal ions.[37–39] Schiff base architectures produce remarkable selectivity, sensitivity, and stability for a particular ion, in addition to provide geometric control over host–guest interactions such as hydrogen bonding, metal-receptor coordination, electrostatic force, van der Waals forces, and hydrophobic interactions.[40,41]

Diaminomaleonitrile (DAMN) derivatives are very good reagents in organic chemistry. They have been used as precursors for synthesizing a broad range of amino-functionalized macrocycles and many other imine compounds.[42,43] Remarkably, DAMN-based ligands are scanty in the literature, and only a few such crystal structures have been reported.[44,45]

Quinoline is well-known as a good fluorophore and chromophore because quinoline and its derivatives have many advantages, such as good coplanarity of the conjugated system, strong intramolecular charge-transfer, excellent solubility, stability and amenability to structural modification. Another important feature of quinoline chemosensors is that they use low-energy two-photon laser as the exciting source, which can reduce cell damage but their applications in fluorescent chemosensors are little investigated.[46–48]

Motivated by the aforementioned data and as a component of our current investigation,[49–51] we have developed and produced a new mono-condensed Schiff base chemosensor (**L**) through the condensation of diaminomaleonitrile and 4-quinoline carboxaldehyde. The backdrop technique used in the chemoreceptor's creation is based on two fundamental ideas. First, the flexibility of the chemosensor would enable the right metal cations to be coordinated. Second, the presence of several chromophoric moieties may result in the production of an appropriate visual signal. The suggested chemosensor (**L**) can use both colorimetric and fluorescence quenching techniques to specifically detect Pb^{2+} ions in an aqueous medium.

2 Experimental

2.1 General information

On a Shimadzu UV 1800 spectrophotometer, UV/visible spectra were recorded using a quartz cuvette with a 10 mm path length. In relation to TMS, the chemical shifts are denoted as δ values (ppm). Using CD_3OD, TMS, and a Bruker Ultrashield 400 instrument, room temperature ^1H and ^{13}C NMR spectra were acquired. ESI-MS spectra were obtained on a mass spectrometer from Waters using triple distilled water and mixed solvent HPLC methanol. For the pH readings, a Merck digital pH meter was employed. Merck provided all of the acquired chemicals and metal salts. Tests should be performed prior to using any salts, including nitrate, that have been re-crystallized from water (Millipore). Solutions of the receptor **L** (1×10^{-5} M) and cations (1×10^{-4}) were prepared in $CH_3OH–H_2O$ (1 : 1, v/v) and H_2O, respectively.

2.2 Synthesis of 2-amino-3-((*E*)-quinolin-4-ylmethyleneamino)maleonitrile (L)

It was synthesised by following a similarly documented process.[52] Typically, 0.316 mg (2 mmol) of 2,3-diaminomalenonitrile in 50 mL of distilled methanol was combined with 0.314 g (2 mmol) of quinoline-4-carbaldehyde in a well-stirred solution. While keeping the environment dry, the resultant pale yellowish solution was refluxed for six hours. The reaction mixture was then allowed to cool to room temperature. A crystalline substance that was off-white emerged. Following filtering, it was allowed to air dry. After that, ethanol was used to recrystallise it, yielding an 85% yield of the yellow-colored chemical. The melting point was above 200 °C. ^1H NMR (400 MHz, CD_3OD, TMS): δ 7.93 (s, –HC=N, 1H), 7.03 (d, 2H, phenyl proton), 5.1 (s, 1H, –OH), 3.77 (s, $–OCH_3$, 6H), 3.68 (s, 2H, NH_2) (Fig. S1†). ^{13}C NMR (400 MHz, CD_3OD, TMS): 192.5, 149.4, 143.2, 127.1, 119.3, 116.2, 113.8, 107.3, 106.4 and 55.4 (Fig. S2†). FTIR/cm^{-1} (KBr): 500 (m), 785 (m), 970 (s), 1329 (s), 1625 ($\nu s.$, –C=N), 2208 (s, –C≡N), 2967 (w), 3300 (m) (Fig. S3†). ESI MS: 248.1195 (LH^+, 30%) (Fig. S4†). Anal. calc. for $C_{14}H_9N_5$: C, 68.01; H, 3.67; N, 28.32. Found C, 68.13%; H, 3.57%; N, 28.46%. Single crystals obtained from the slow evaporation of the methanolic solution were found suitable for X-ray analysis.

2.3 Preparation and characterization of the lead complex of L (1)

Dropwise, while stirring, **L** (0.124 g, 0.5 mmol) in methanol (20 mL) was added to a methanol solution (10 mL) containing

$Pb(NO_3)_2$ (0.165 g, 0.5 mmol). After three more hours of stirring the mixture, the yellow precipitate was filtered out and washed with methanol and hexane. Yield, 0.166 g (68%). FTIR/cm^{-1} (KBr): 510 (m), 590 (s), 778 (*vs.*), 1355 (*vs.*, NO_3^-), 1566 (s), 1610 (*vs.*, –C=N), 2195 (s, –C≡N), 2515 (vb), 3220 (b, –NH) (Fig. S5†). EI-MS: $m/z = 490.7767$ ($\mathbf{L} + Pb^{2+} + 2H_2O$) (Fig. S6†). UV-vis λ_{max}/nm (CH_3OH): 296 nm, 368 nm. Λ_M/Ω^{-1} cm^{-2} mol^{-1} (CH_3OH): 195 (1 : 2 electrolyte). Anal. calc. for $C_{14}H_{13}N_5O_2Pb$: C, 34.28; H, 2.67; N, 14.28%. Found C, 34.36%; H, 2.59%; N, 14.35%.

2.4 X-ray single crystal data collection and structural determination

MoKα ($\lambda = 0.7107$ Å) radiation was used to gather X-ray single crystal data on a BRUKER APEX II diffractometer with a CCD area detector. Data reduction, data collection, and structural solution/refinement were performed using the SMART APEX software.[53] Both direct approaches (SHELXS-97) and standard Fourier methods were used to solve the structures. The SHELX-97 software,[54] which was incorporated into WinGX,[55] was then utilised to refine the structures on F2 by full matrix least squares techniques (SHELXL-97). In most of the examples, anisotropic interactions were seen with non-hydrogen atoms. The hydrogen atoms were geometrically held in a place according to the riding atom model. Table 1 contains the probe **L**'s crystallographic data. A repository of structural data is available at the Cambridge Crystallographic Data Centre (CCDC 2294084). Bond distances and bond angles of **L** are given in Tables S1 and S2.†

Table 1 Crystallographic data and structure refinement parameters of receptor L

CCDC number	2294084
Empirical formula	$C_{14}H_9N_5$
Formula weight	247.25
Temperature/K	293(2)
Crystal system	Monoclinic
Space group	$P2_1/c$
a/Å	10.4775(3)
b/Å	7.5290(3)
c/Å	15.5021(5)
α/°	90
β/°	94.249(3)
γ/°	90
Volume/Å^3	1219.52(7)
Z	3
ρ_{calc}/g cm^{-3}	1.464
μ/mm^{-1}	0.089
F(000)	558.0
Crystal size/mm^3	31 × 14 × 25
Radiation	Mo Kα ($\lambda = 0.71073$)
2θ range for data collection/°	3.898 to 54.23
Index ranges	$-13 \le h \le 9, -9 \le k \le 9, -19 \le l \le 19$
Reflections collected	12 049
Independent reflections	2540 [$R_{int} = 0.0450, R_{sigma} = 0.0362$]
Data/restraints/parameters	2540/0/172
Goodness-of-fit on F^2	1.098
Final R indexes [$I >= 2\sigma(I)$]	$R_1 = 0.0393$, w$R_2 = 0.1018$
Final R indexes [all data]	$R_1 = 0.0549$, w$R_2 = 0.1087$
Largest diff. peak/hole/e Å^{-3}	0.14/−0.17

2.5 UV-vis titrations

By diluting 30 μL of the dissolved **L** (2.47 mg, 0.01 mmol) with the solvent mixture $CH_3OH–H_2O$ (1 : 1, v/v) (10 mL), a final concentration of 10 μM was obtained. The guest cations solution was prepared separately by diluting nitrate salts (between 10 mM) with triple distilled water up to the necessary concentration. UV-vis spectra were obtained after combining **L** with each metal ion for a short while at room temperature.

2.6 Fluorescence titration

$Pb(NO_3)_2$ (33.1 mg) was dissolved in triple distilled water (10 mL), and 1.5–90 μL of this Pb^{2+} solution (10 mM) was transferred to each receptor solution (10 μM) to give 0.5–30 equiv. **L** (2.47 mg, 0.01 mmol) was dissolved in the above-mentioned solvent (10 mL) to make a solution, and 30 μL of this solution was diluted with 3 mL of the solvent mixture to prepare a final concentration of 10 μM. The fluorescence spectra were collected at room temperature after a brief period of mixing.

2.7 Job plot measurements

L (2.47 mg, 0.01 mmol) was measured and added to 10 mL of methanol for dissolution. Vials were filled with 100, 90, 80, 70, 60, 50, 40, 30, 20, 10, and 0 μL of the **L** solution. A mixture solvent (2.9 mL) was added to each vial to dilute it. Triple distilled water (10 mL) was used to dissolve $Pb(NO_3)_2$ (0.01 mmol). For every diluted **L** solution, 0 μL, 10, 20, 30, 40, 50, 60, 70, 80, 90, and 100 μL of the Pb^{2+} solution were added. The total capacity of each vial was 3 mL. At room temperature, UV-vis spectra were collected after a minute of shaking.

2.8 pH effect test

A range of buffers with pH values between 2 and 12 were prepared using 100 mM HEPES buffer. After the solution's pH was reached, Receptor **L** (2.47 mg, 0.01 mmol) was dissolved in 10 mL of methanol. Using the previously mentioned buffers, 30 μL of this solution (1 mM) was diluted to 3 mL in order to obtain a final concentration of 10 μM. $Pb(NO_3)_2$ (33.1 mg, 0.1 mmol) was dissolved using the HEPES buffer (10 mL, pH 7.00). Thirty μL of the Pb^{2+} solution (10 mM) was added to each 10 μM receptor solution that had previously been prepared. After a short mixing time, fluorescence spectra were recorded at room temperature.

3 Results and discussion

3.1 Synthesis and structure of the probe

The organic ligand, 2-amino-3-((*E*)-quinolin-4-ylmethyleneamino)maleonitrile (**L**) was prepared in good yield (85%) by the condensation reaction of 1 : 1 Schiff-base of 2,3-diaminomaleonitrile and 4-quinoline carboxaldehyde in 1 : 1 mole ratio in anhydrous methanol solvent (Scheme 1), and characterized by ^{1}H NMR and ^{13}C NMR, IR and EI-MS spectroscopy, single crystal XRD analysis, elemental analysis, and DFT studies. The IR spectrum of the mono Schiff base **L** showed a broad band at 3300 cm^{-1} for NH stretching vibration.

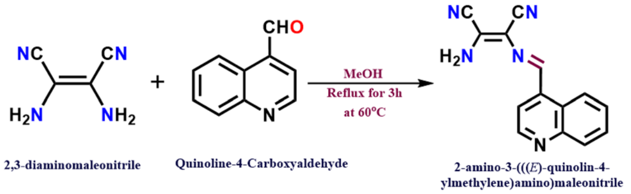

Scheme 1 Synthetic procedure of receptor **L**.

Furthermore, the band observed at 1625 cm^{-1} can be ascribed to the stretching frequency of γ(C=N). At 2208 cm^{-1}, the vibration produced by the nitrile groups (–C≡N) is visible.

The molecule **L** was subjected to DFT computations. Starting from the Gauss-view structure of **L**, the geometry optimisation results in a global minimum. Fig. 1 depicts the optimised structure of the **L**. Fig. 2 shows the outlines of a few chosen HOMO and LUMO orbitals of **L** as well as a schematic representation of the energy of MOs. The HOMO to LUMO energy gap for **L** is 1.9340 eV.

The light yellow rod-shaped single crystals of X-ray quality of the **L** were crystallized in a 'monoclinic' space group $P2_1/c$ from the methanol solvent system by slow vaporisation at room temperature. In unit cell there are four symmetry generated molecules of **L** (Fig. 3). The quinoline and maleonitrile fragments are not in the same plane but in a torsion angle of −174.04°. It creates a dimer through the hydrogen bond (distance 2.124 Å) between the quinoline N atom of one molecule with the amine hydrogen atom of another molecule (Fig. S7†). There is a presence of strong C–H⋯Π interaction [C⋯Π center distance = 3.294 Å; ∠C–H⋯Π center = 85.76° along axis-*c*] which produces the overall lattice packing. The C–CN angles in **L** lies between 177.96 to 178.88° (almost linear).

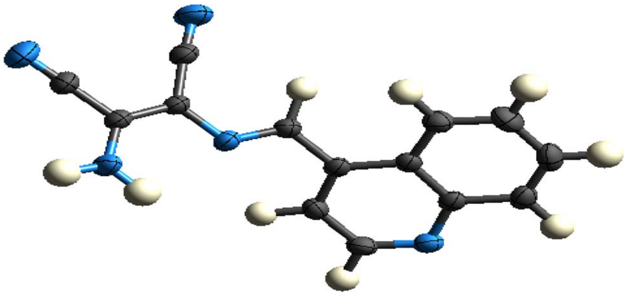

Fig. 3 ORTEP plot of L showing 50% probability.

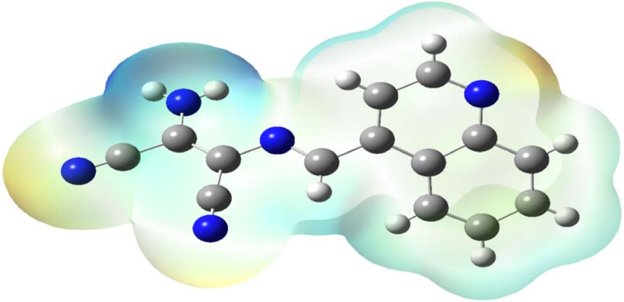

Fig. 4 Molecular electrostatic potential diagram of L.

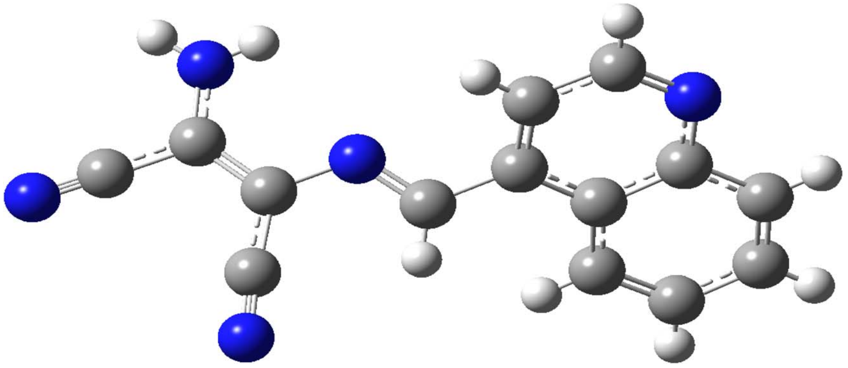

Fig. 1 Diagram of the optimised geometry of molecule L.

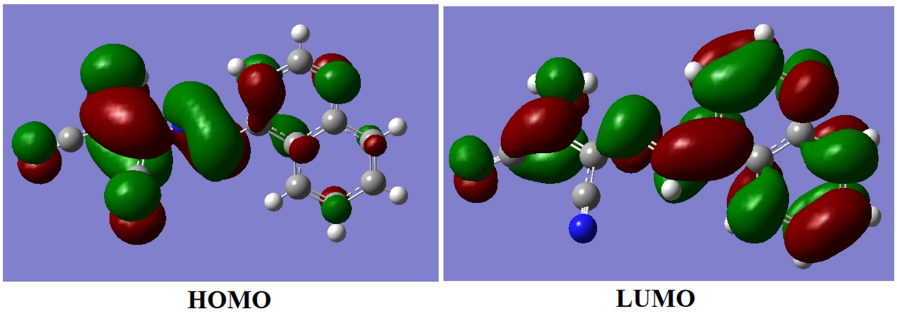

Fig. 2 HOMO and LUMO contour diagrams for L.

3.2 Molecular electrostatic potential (MEP)

The potential rises in the following order: red, yellow, green, blue, pink, and white. The regions with the highest negative electrostatic potential, which are associated with electrophilic reactivity, are shown in red and yellow, and the highest positive electrostatic potential, which is associated with nucleophilic reactivity, is represented in white, and the region with the lowest potential is represented by blue. The molecular electrostatic potential (MEP) of ligand **L** is shown in Fig. 4.

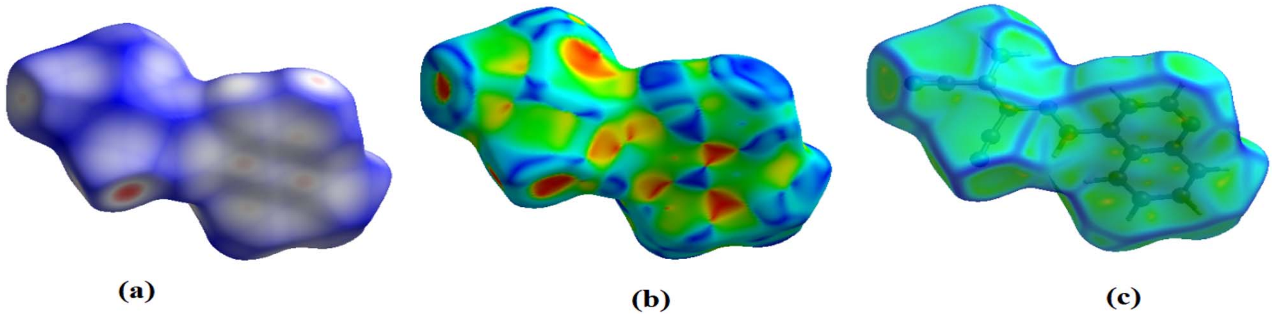

Fig. 5 Hirshfeld surfaces of **L**: (a) 3D d_{norm} surface, (b) shape index, and (c) curvedness.

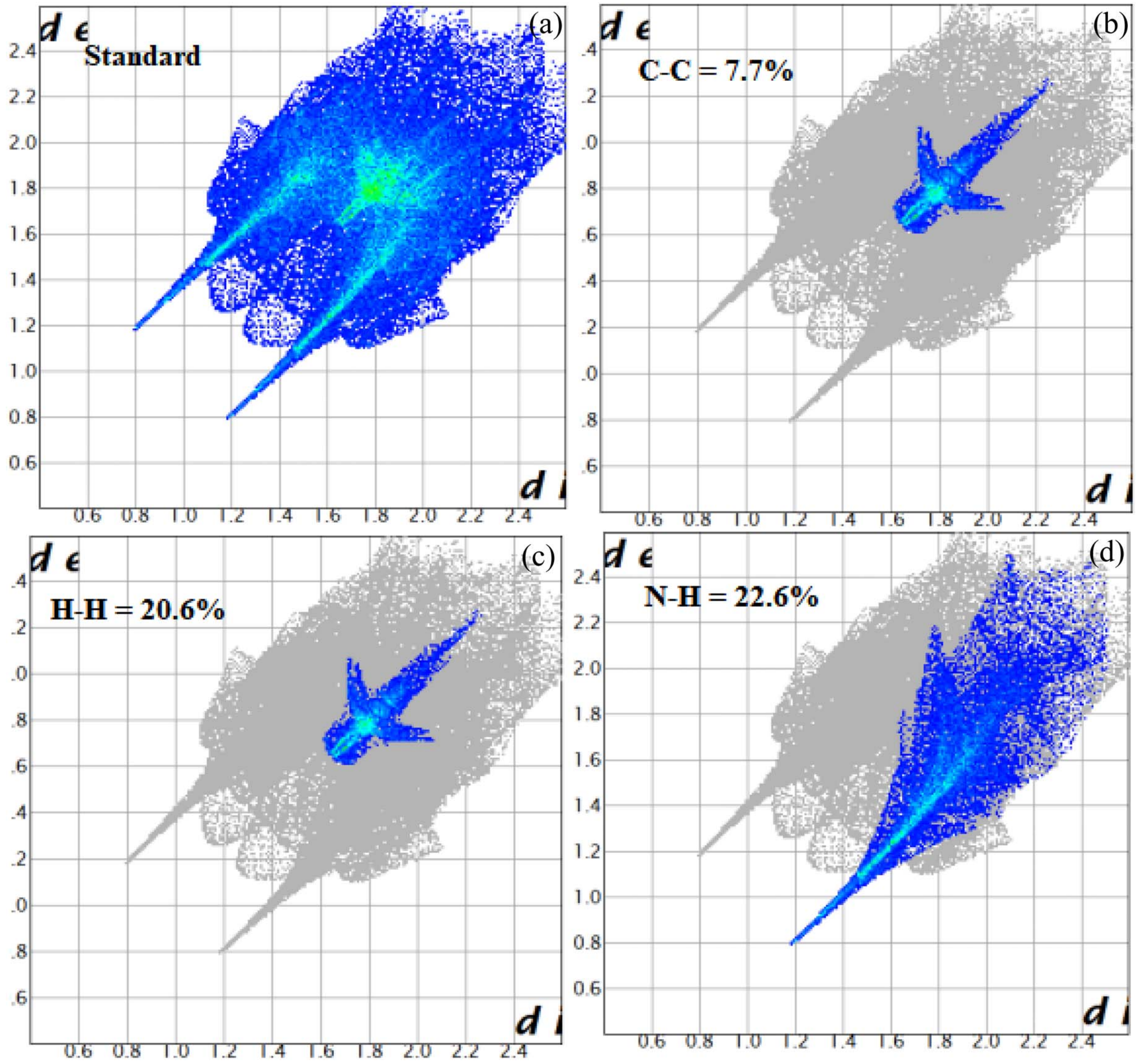

Fig. 6 2D fingerprint plots of ligand **L**: (a) standard full, (b) resolved into C⋯C, (c) resolved into H⋯H and (d) N⋯H contacts, showing the percentages of contacts contributing to the total Hirshfeld surface area of the molecule.

3.3 Molecular Hirshfeld surfaces

The Hirshfeld surface is a helpful method for describing the characteristics of a molecule's surface. The molecular Hirshfeld surface of **L** was created by mapping the 3D d_{norm} surfaces across a predetermined colour scale of −0.5033 (red) to 1.2212 Å (blue) using a standard (high) surface resolution. Whereas Shapeindex was mapped between −1.00 and +1.0 in colour, curvedness was mapped between −4.0 and +4.0. The surfaces were shown to be transparent, allowing the molecular moiety to be visualised in a constant orientation for each structure around which they were calculated. The molecular Hirshfeld surface (d_{norm}, shape index, and curvedness) of **L** is shown in Fig. 5.

The intermolecular interactions that were most common were H⋯H and N⋯H, according to the Hirshfeld surface analysis of ligand **L**. The corresponding C⋯C, H⋯H, C⋯H, and N⋯H interactions were 7.7%, 20.6%, 13.5%, and 22.6%, respectively. A small area on the right side of the top of the 2D fingerprint map almost equally represented the C⋯C and C⋯H interactions, whereas the N⋯H interactions were represented by the largest in the fingerprint plot (Fig. 6) and therefore had the most significant contribution to the total Hirshfeld surfaces (22.6%).

3.4 Effects of solvents on the fluorescent spectra of the chemosensor L

Since the solvent system has a significant impact on the chemosensor fluorescence intensity, appropriate solvents were used for this experiment. Thus, the excitation wavelength for the chemosensor **L** fluorescence intensity test was set at 340 nm. The results of the experiment showed that the methanol solvent had the strongest fluorescence emission intensity, which was centred at 400 nm of **L**. The fluorescence of the other solvents was a bit weaker, as shown in Fig. 7. For the subsequent investigations, methanol was chosen as the solvent.

3.5 A visual study of chemosensor L for versatile metal ions

The colorimetric tests of chemosensor **L** in alcoholic media were conducted using various monovalent, divalent, and trivalent cations, including Ag^{+}, Zn^{2+}, Pb^{2+}, Mn^{2+}, Cu^{2+}, Ca^{2+}, Ba^{2+}, Mg^{2+}, Sr^{2+}, Fe^{2+}, Ni^{2+}, Co^{2+}, Cd^{2+}, Hg^{2+}, Cr^{3+}, Fe^{3+}, Gd^{3+}, Sm^{3+}, and Al^{3+}. In methanol, chemosensor **L** exhibits a yellow colour. The addition of other cations to the 1 : 1, v/v methanol–water mixture did not significantly alter the colour of chemosensor **L**, with the exception of the Pb^{2+} ion (Fig. 8). This implies that the chemosensor **L**'s high sensitivity and selectivity were restricted

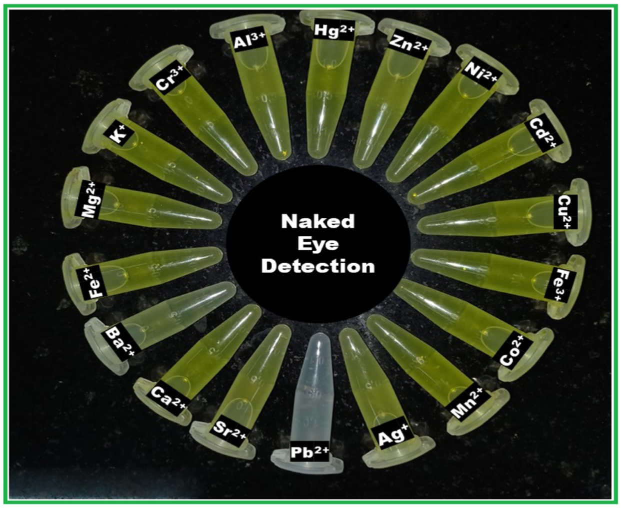

Fig. 8 Naked-eye presentation of chemosensor L with different metal ions.

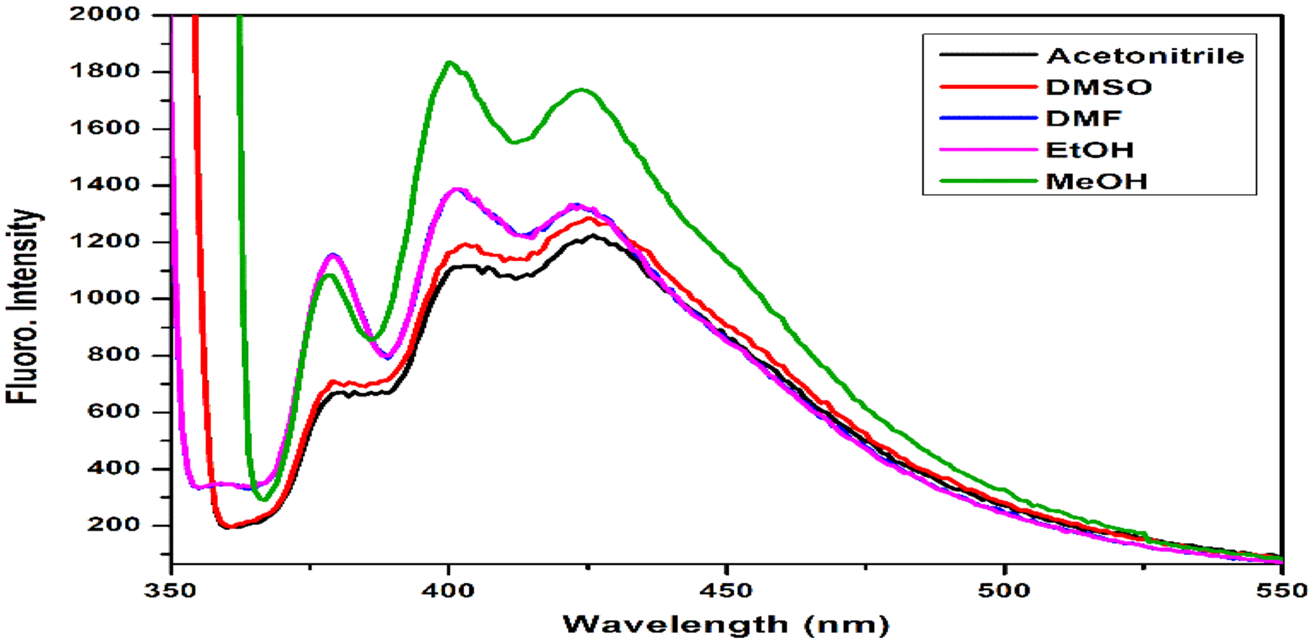

Fig. 7 Effects of different solvents on the fluorescence intensity of the chemosensor L.

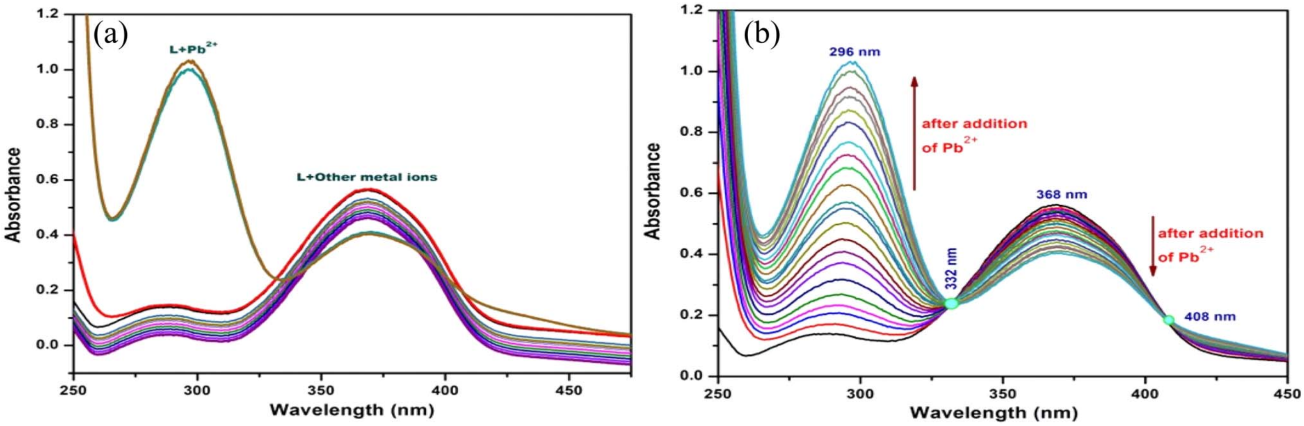

Fig. 9 (a) UV-vis spectra of **L** in the presence of various metal ions (Hg^{2+}, Zn^{2+}, Ni^{2+}, Fe^{2+}, Cd^{2+}, Cu^{2+}, Fe^{3+}, Co^{2+}, Mn^{2+}, Ag^{+}, Sr^{2+}, Ca^{2+}, Ba^{2+}, Mg^{2+}, Sm^{3+}, Gd^{3+}, Cr^{3+}, Al^{3+} and Pb^{2+}). (b) UV-vis spectra of **L** upon adding 0–1.2 equivalent of Pb^{2+} ion ($[\mathbf{L}] = 1 \times 10^{-3}$ mol L^{-1}, solvent: 1 : 1 MeOH-H_2O, pH = 7.27, $\lambda_{max} = 368$ nm). When 1.2 equiv. of Pb^{2+} ions are added, the peak of the free chemosensor **L** (centred at 368 nm) vanishes and the absorption band at 296 nm increases with a blue shift. This is because Pb^{2+} coordinates with the free amine group and azomethine N (–C=N–) of the receptor **L**. Chemosensor **L** did not exhibit any significant spectral changes in the alcoholic medium upon the addition of additional metal ions (Hg^{2+}, Zn^{2+}, Ni^{2+}, Fe^{2+}, Cd^{2+}, Cu^{2+}, Fe^{3+}, Co^{2+}, Mn^{2+}, Ag^{+}, Sr^{2+}, Ca^{2+}, Ba^{2+}, Mg^{2+}, Sm^{3+}, Gd^{3+}, Cr^{3+}, and Al^{3+}). The development of complex species between **L** and Pb^{2+} was shown by clear isosbestic points at 408 nm and 332 nm (b). The molar extinction coefficient of the new peak at 296 nm is 18.5×10^4 M^{-1} cm^{-1}, which is too large for Pb-based d–d transitions and thus must correspond to metal–ligand transitions. As there are blue shifts in the absorption spectra of Pb^{2+} with the chromophore **L**, there are chances for ligand-to-metal charge transfer (LMCT) and the formation of a complex between the receptor **L** and Pb^{2+}.

to Pb^{2+} ions. The decolorisation of chemosensor **L** is brought on by the azomethine group's (–C=N–) preferential attachment to the metal ion. As a result, this procedure produces very high selectivity.

3.6. UV-vis spectroscopic studies of the probe L

The UV-vis absorption studies of **L** were performed in the presence of different cations such as Ag^{+}, Zn^{2+}, Pb^{2+}, Mn^{2+}, Cu^{2+}, Ca^{2+}, Ba^{2+}, Mg^{2+}, Sr^{2+}, Fe^{2+}, Ni^{2+}, Co^{2+}, Cd^{2+}, Hg^{2+}, Cr^{3+}, Fe^{3+}, Gd^{3+}, Sm^{3+}, and Al^{3+}. The chemosensor **L** displayed two absorption bands centered at 368 nm and a shoulder at 290 nm (Fig. 9). The absorption bands at 368 nm and 296 nm correspond to the π–π* and n–π* transitions, respectively.

3.7 Fluorescence spectroscopic studies of the probe L

The chemosensor **L** showed fluorescence spectra with excitation wavelength 340 nm and strong emission displayed at two close maximas at 400 nm and 425 nm (Fig. 10a). The emission studies of **L** were also investigated in the presence of different cations such as Hg^{2+}, Zn^{2+}, Ni^{2+}, Fe^{2+}, Cd^{2+}, Cu^{2+}, Fe^{3+}, Co^{2+}, Mn^{2+}, Ag^{+}, Sr^{2+}, Ca^{2+}, Ba^{2+}, Mg^{2+}, Sm^{3+}, Gd^{3+}, Cr^{3+}, and Al^{3+}, same as those in the UV-vis studies. After the addition of other metal ions

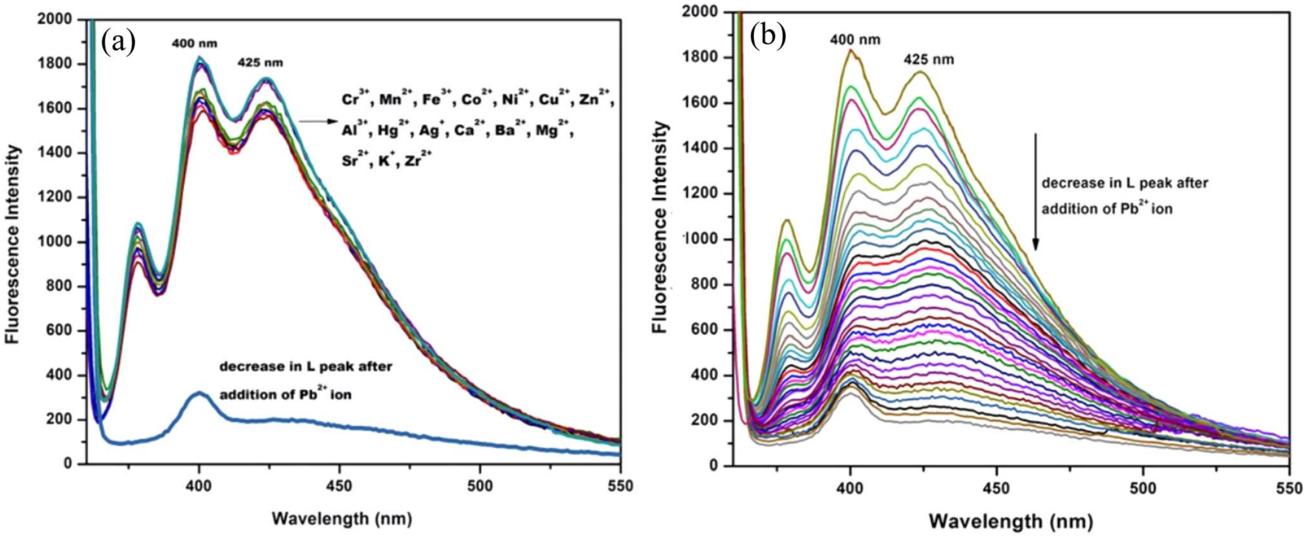

Fig. 10 (a) Emission spectra of **L** in the presence of various metal ions (Hg^{2+}, Zn^{2+}, Ni^{2+}, Fe^{2+}, Cd^{2+}, Cu^{2+}, Fe^{3+}, Co^{2+}, Mn^{2+}, Ag^{+}, Sr^{2+}, Ca^{2+}, Ba^{2+}, Mg^{2+}, Sm^{3+}, Gd^{3+}, Cr^{3+}, and Al^{3+}). (b) Fluorescence titration plot of **L** upon adding 0 to 1.2 equiv. of Pb^{2+} ion ($[\mathbf{L}] = 1 \times 10^{-3}$ mol L^{-1}, CH_3OH/H_2O = 1 : 1, v/v, $\lambda_{ex} = 340$ nm).

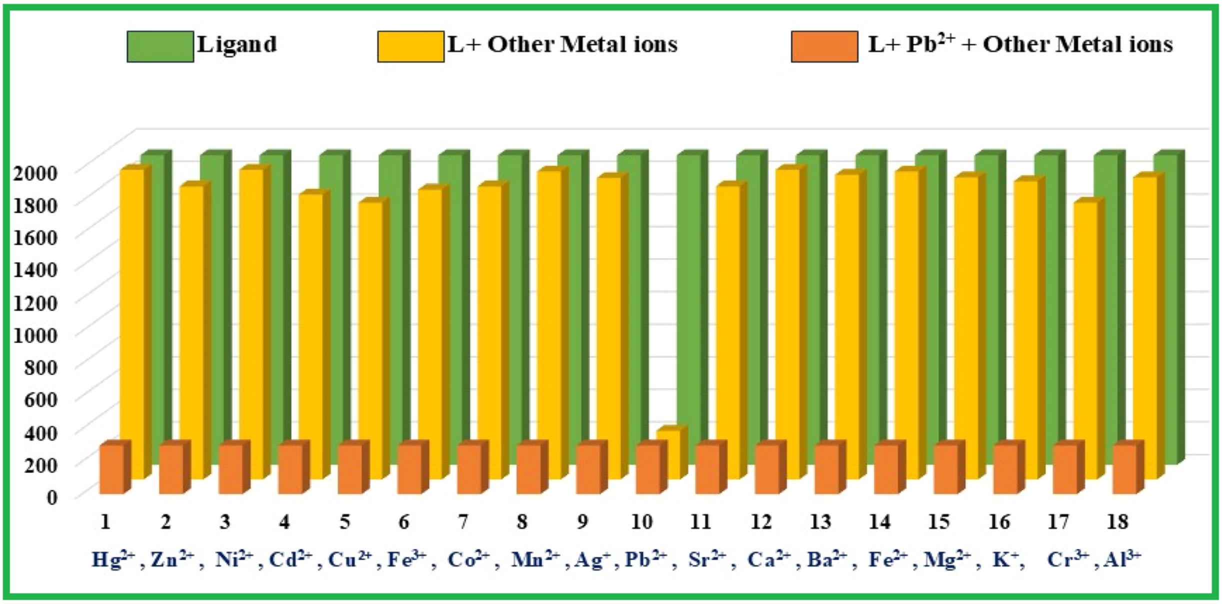

Fig. 11 Competitive experiment of L (10 μM) with Pb^{2+} (1.2 equiv.) in presence of other metal ions.

emission spectra did not change significantly, but in the presence of Pb^{2+} smooth quenching was observed up to 90%. This indicates that the chemosensor **L** has a single and efficient recognition of the metal Pb^{2+} ion, which is shown below. The fluorescence titration plots are provided in Fig. 10b.

3.8 Anti-interference studies of the probe L

Next, using the fluorescence tests under the same experimental conditions, the chemosensor **L**'s particular Pb^{2+} ion selective responses were examined. When comparable concentrations of other major competing cations coexist with Pb^{2+} ions, separately, the quenched fluorescence intensity of the guest-bound receptor at 400 nm remains unaffected. The anti-interference behaviour persisted even at concentrations of the background cations up to two times higher than those of the analytes, as demonstrated by the absence of an additional peak or the disappearance of the host–guest complex's original peak (Fig. 11).

3.9 Absorbance and fluorescent detection limits

The colorimetric and fluorometric detection limits obtained from the UV-vis and emission titration curves calculated by the standard formula $3\sigma/s$ were found to be 1.2×10^{-6} M and 9.9×10^{-7} M, respectively, for Pb^{2+}ions (Fig. 12), which are far below the WHO guidelines for drinking water. Thus, the chemosensor **L** can be applicable as a visual colorimetric probe towards Pb^{2+} at physiological conditions.

3.10 Determination of binding constant

The binding mode was calculated from the job's plot, which revealed that the stoichiometric ratio of **L** with Pb^{2+} is 1 : 1 (Fig. S8†). The fluorescence binding constant was also calculated using the Benesi–Hildebrand equation and was found to be 5.63×10^3 M (Fig. 13a). The fluorescence quenching constant was calculated using the Stern–Volmer plot, and the estimated

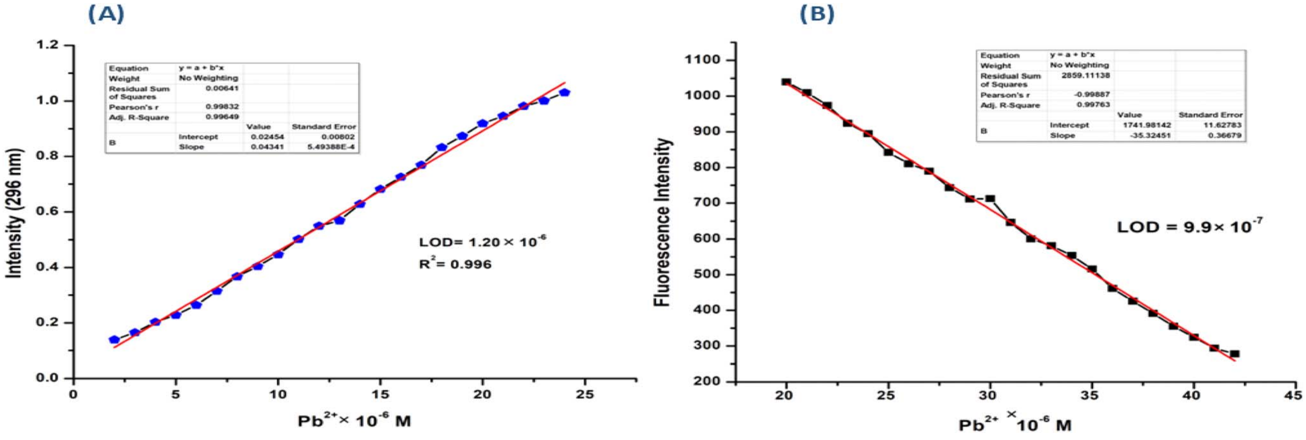

Fig. 12 (A) Detection limit of L for Pb^{2+} by UV-Vis spectroscopy (inset: Intercept and slope of the calibration curve) and (B) detection limit of L for Pb^{2+} by fluorescence spectroscopy (inset: Intercept and slope of the calibration curve).

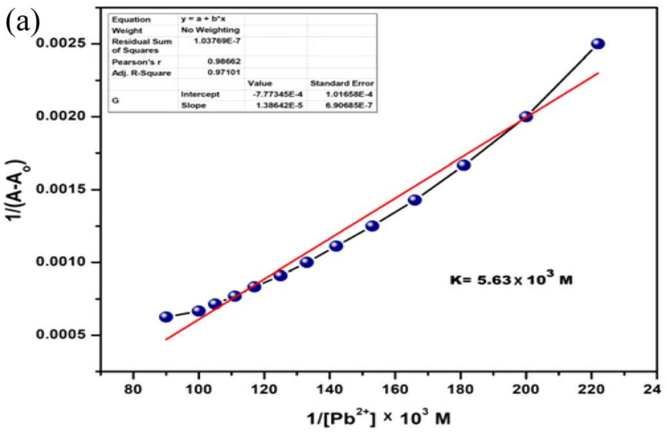

Fig. 13 (a) Binding constant using Benesi–Hildebrand equation through UV-Vis measurements (inset: Intercept and slope of the calibration curve) (b) fluorescence quenching constant using Stern–Volmer equation [inset: Intercept of the calibration curve and Co-efficient of determination (R_2)].

quenching constant (k_{sv}) of the **L**–Pb^{2+} complex was found to be 6.7 × 10^3 M (Fig. 13b). It revealed the high quenching efficiency and high selectivity of **L** towards Pb^{2+} ion in the methanol medium.

3.11 pH effect

To assess the chemosensor **L**'s suitability for real-world uses in environmental and agricultural samples, the impact of pH on its fluorescence profile was examined. The pH range for the absorption and emission studies was 2.0–13.0, and the fixed concentrations of chemosensor **L** (2.0 µg mL^{-1}) and Pb^{2+} ion (3.0 µg mL^{-1}) were used. The findings demonstrated that in the pH range of 2.0–7.0, both absorbance and fluorescence intensity increased significantly. The intensity of the fluorescence peaked at pH 7, although it continued to decline as pH increased to a range of 8–13. As the metal ions precipitated, the fluorescence intensity progressively dropped (Fig. 14).

3.12 Reversibility test

Stable chelate complexes are typically formed between metal ions such as the Pb^{2+} ion and multidentate ligand Na_2EDTA. Reversibility was confirmed by absorption/fluorescence measurements with Na_2EDTA as the working medium and **L** + M^{2+} (M = Pb) solution. The characteristic emission bands of the host–guest complexes at 400 nm disappeared as soon as the **L** + M^{2+} molecule reacted with one equivalent (Fig. 15). The practically complete recovery of the emission intensity at 400 nm upon the addition of analyte indicates that the sensing process is more reversible than any irreversible reaction facilitated by metals. The chemosensor **L** is reversible up to three cycles (Fig. S9†).

3.13 Time-dependence test

Additionally, a time-resolved analysis of the variations in **L**'s fluorescence intensities in the presence of 1.2 equivalents of Pb^{2+} was conducted (Fig. S10†). After a few minutes of adding Pb^{2+} ions to **L**, the fluorescence intensity dropped quickly and reached the steady minimum level (94% decrease in the fluorescence intensity). Consequently, prior to measurements in subsequent research, all solutions were stored for a minimum of one to two minutes. Over an extended length of time (up to a week), the fluorescence properties of **L** in the absence of Pb^{2+} remained unchanged.

3.14 Sensing mechanism

To gain a deeper understanding of the sensing mechanism, **L**–Pb^{2+} adduct mass spectral and infrared spectral experiments

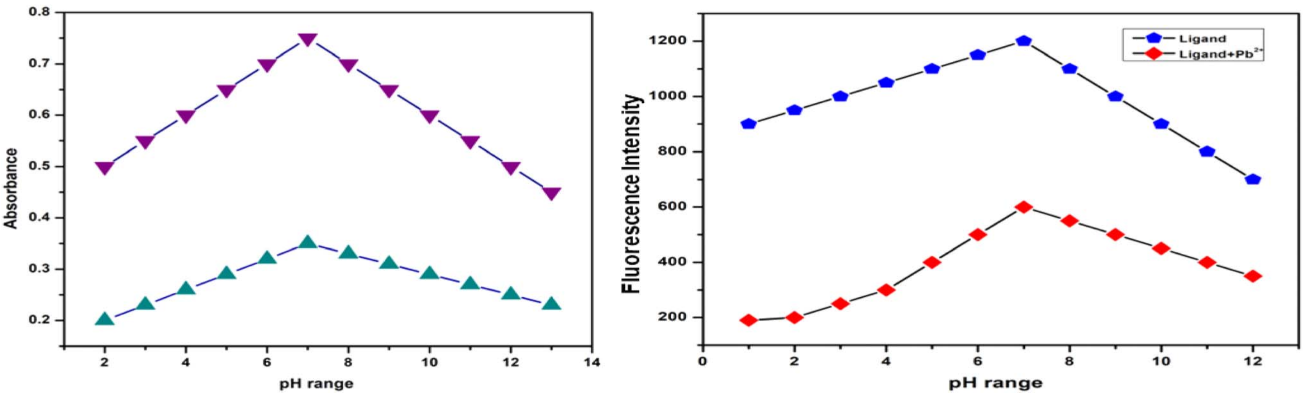

Fig. 14 Effect of pH (range 2–13) on **L** in UV-vis and fluorescence spectroscopy.

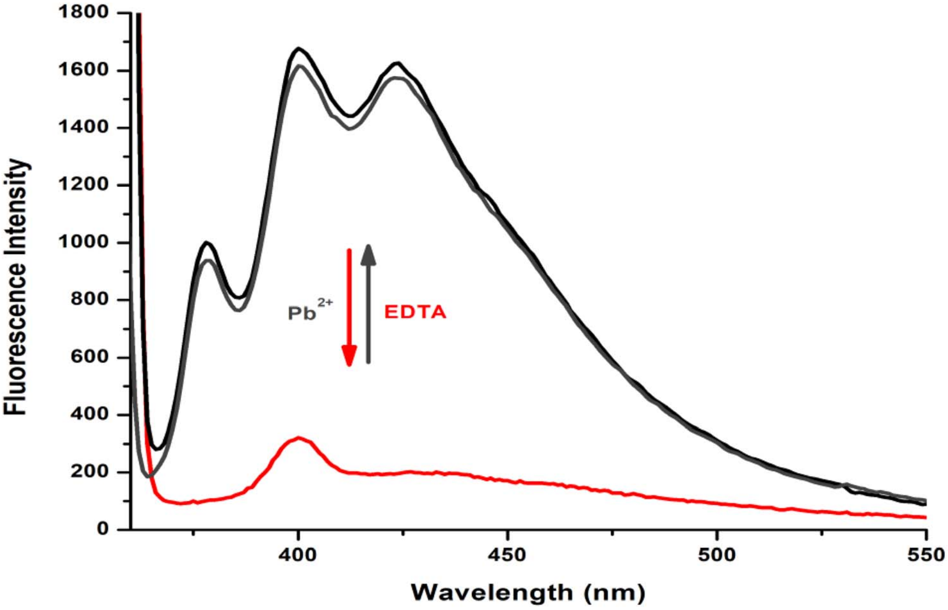

Fig. 15 Reversibility of L–Pb^{2+} with Na_2EDTA using fluorescence spectroscopy at 400 nm.

were conducted. A peak at $m/z = 490.7767$ appears in the ESI-mass spectra of the **L**–Pb^{2+} adduct, which can be attributed to [**L** + Pb^{2+} + $2H_2O$] (Fig. S6†). The C═N groups imine moiety is responsible for the very sharp band that is centred at 1625 cm^{-1} in the infrared spectra of the free ligand **L**. This band moved to 1610 cm^{-1} in the Pb^{2+} complex of **L**, indicating a shift towards lower wave numbers and the potential involvement of the azomethine group in the interaction of the metal ions with the ligand. Additionally, the other peaks caused by ligand **L**'s –NH and –CH groups shrank and moved to lower wave numbers (Fig. S11†). The primary cause of metal sensing is the detection of the binding site and signal transduction pathway by the analyte. While the quinoline unit functions as a signalling subunit, the imine-attached quinoline moiety and the free amine end of the maleonitrile moiety comprise a pocket appropriate for metal coordination. Beginning with the absorption spectra, high blue shift absorption indicates complexation at the acceptor site, which in the ground state enhances the ICT process and results in colorimetric sensing. In the excited state, fluorometric sensing is caused by both the PET and the ICT effect. Scheme 2 displays the binding mechanism. The binding mechanism was also confirmed by the ^{1}H-NMR titration. On gradual addition of Pb^{2+} ions, the peaks of the free NH_2 group and –NH group (δ = 3.68 and 7.93 ppm, respectively) in the probe **L** diminished and upon 1 equivalent addition of Pb^{2+} ions, these two peaks completely vanished along with slight down-filed shifts of the other protons (Fig. S12†).

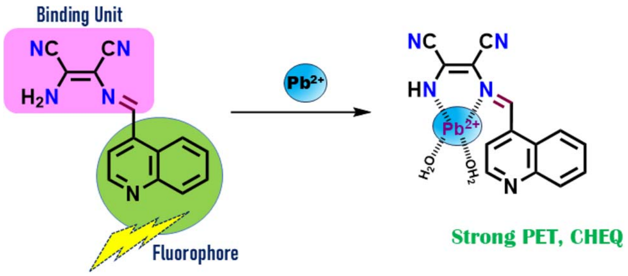

Scheme 2 Probable sensing mechanism.

3.15 DFT studies on the metal complexes

Density functional theory (DFT) simulations of the Pb^{2+} complex of the ligand **L** {**1**} were carried out in order to obtain a close approach to the likely binding mechanism. Fig. S13† displays the geometry-optimized structures, a schematic depiction of the energy of MOs, and the contours of particular HOMO and LUMO orbitals of the **L**–Pb^{2+} complex. Significantly, the estimated energy gaps between LUMO and HOMO dropped from its Pb^{2+} complex (1.2930 eV) to **L** (1.9340 eV). The

Table 2 Determination of Pb^{2+} ions in different water samples

Metal ion	Spiked amount (μM)	Recovered amount (μM)	% recovery ± D ($n = 3$)
Pb^{2+}	5.00	5.08	101.8 ± 0.35
	10.00	9.98	99.8 ± 0.69
	20.00	19.96	99.2 ± 0.55

chemosensor **L**'s HOMO–LUMO energy gaps were lowered upon Pb^{2+} complexation, and this was ascribed to the electron redistributions that changed the absorbance and fluorescence spectra.

4 Application

4.1 Real sample analysis

The chemosensor **L** was used successfully to identify Pb^{2+} ions in a range present in water samples. For this reason, distinct Pb^{2+} ion-contaminated samples were created by spiking different known concentration levels. After that, their concentrations were examined using the previously indicated sensing apparatus. The experiment showed a good recovery with a very low standard deviation after three cycles. The results are shown in Table 2.

4.2 Analysis of biological samples

In order to evaluate the efficacy of the chemosensor **L** in biological samples, Pb^{2+} was successfully detected in an aqueous solution of bovine serum albumin (BSA) protein using the probe **L** of conc. 10 mM. Pb^{2+} was added to the bovine serum albumin (BSA) medium one at a time, and each time the fluorescence intensity dropped. There was an almost 30-fold quenching of the emission intensity when Pb^{2+} was present (Fig. 16), showing noticeable red shifting when **L** was added, going from 400 nm to 450 nm while quenching was ongoing.

4.3 Logic gate application

A bimolecular logic device can be created by concurrently detecting Pb^{2+} ions using chromo-fluorometric techniques. Supramolecular logic gates react to the introduction of appropriate input guest molecules at both low and high concentrations by changing the optical characteristics of the receptor molecule. These gates function on an extremely tiny scale. The output spectra intensity has binary codes of 0 and 1, respectively. One or both of the receptor solutions' fluorescence amplification at 400 nm and absorption band at 368 nm would be very appreciated and evaluated as 1, and in the low condition of spectral intensity, as 0. This is true for inputs including EDTA or Pb^{2+} ions. Furthermore, the INHIBIT logic function can be utilised to control the same spectrum intensity switching behaviour in the alternate Pb^{2+} addition and EDTA (Fig. 17).

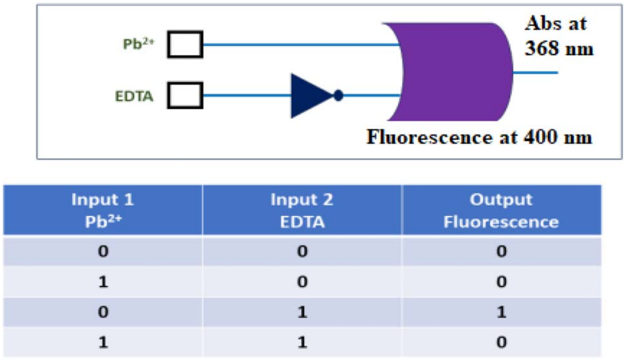

Input 1 Pb^{2+}	Input 2 EDTA	Output Fluorescence
0	0	0
1	0	0
0	1	1
1	1	0

Fig. 17 The logical behavior of L and the corresponding truth table.

5 Comparison of L with other previously reported chemosensors for Pb^{2+} ions

The creation of a novel fluorescent-colorimetric probe **L**, which was verified for Pb^{2+} ion detection and quantification in the aqueous-methanol medium, is described in the current work. This work is a part of our continuous endeavour to offer practical analytical methods that may be used as fast, as cheaply,

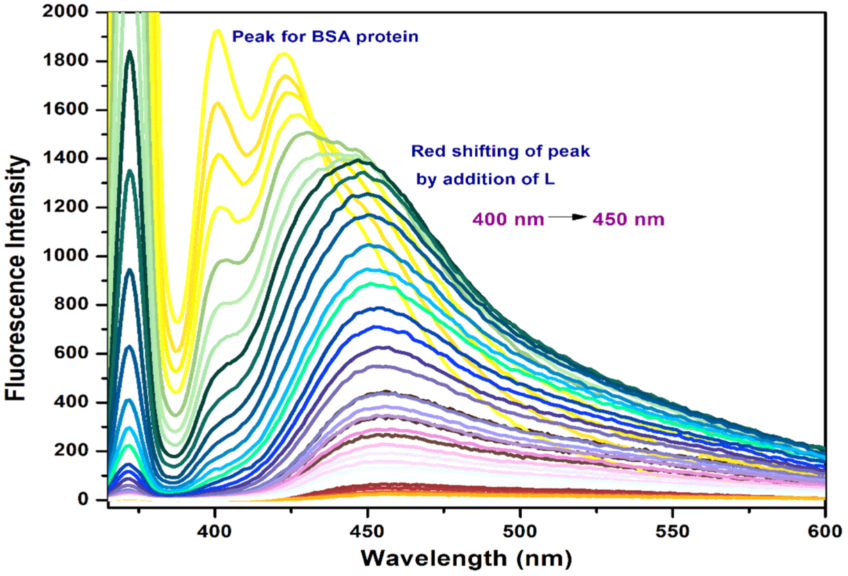

Fig. 16 Fluorescence studies of L in the presence of BSA protein in the aqueous-methanol medium.

Table 3 Comparison of some previously reported chemosensors for Pb^{2+} ions

Structure/name of probe	Solvent/medium	Sensing method	Binding constant	LOD	Ref.
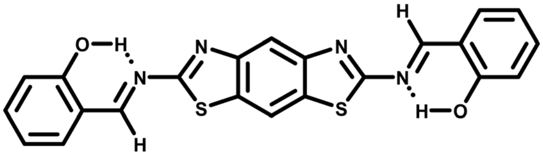	$DMSO/H_2O$ (30 : 70, v/v)	Fluorescence	0.41×10^5	2.23×10^{-6} M	56
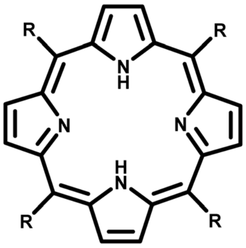	Ethanol	Fluorescence	—	2.2×10^{-8} M	57
1,2,3-Triazole based Schiff base chemosensor	—	UV-visible/ fluorescence	$4.1 \times 10^6\ M^{-1}$	0.25 μM	58
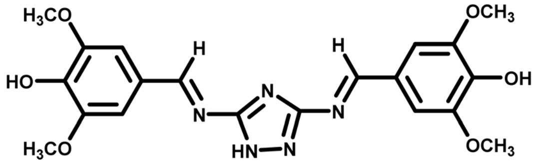	CH_3OH–Tris buffer (1 : 1, v/v)	Colorimetric and fluorescent chemosensor	9×10^5	Colorimetric: 1.2×10^{-6}; fluorometric: 9×10^{-7} M	59
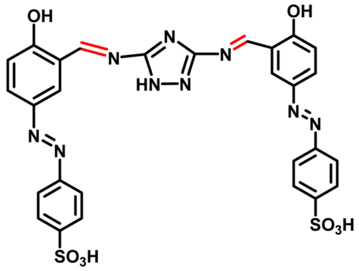	$MeOH–H_2O$	Colorimetric and fluorescent chemosensor	2×10^7	Colorimetric: 1.0×10^{-9} M; fluorometric: 0.53×10^{-9} M	60
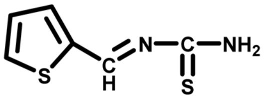	PVC: DOP: LL2: NaTPB	Potentiometric	—	1.0×10^{-7} M	61
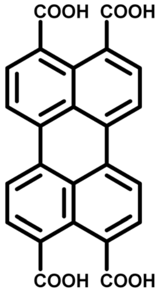	Aqueous medium	Colorimetric and fluorescent chemosensor	—	—	62
Dimeric quinoline-based Schiff base	Methanol	Fluorescent chemosensor	—	1.3×10^{-7} M	63
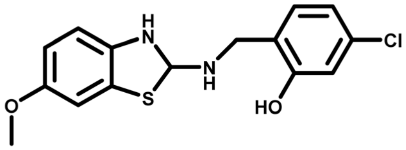	DMSO/Tris–HCl buffer (3 : 7, v/v	Fluorescent chemosensor	—	0.059 μM	64

and as sensitively as possible to monitor the growing number of analytes of environmental concern. Several studies have employed a few triazoles, macrocyclic, and Schiff base-based compounds to selectively detect Pb^{2+} ions. A comparison of the probe L and the reported chemosensors is shown in Table 3. Although the other chemosensors demonstrated certain benefits, such as high sensitivity and selectivity, the key characteristics of the fluorescent-colorimetric chemosensor, **L**, are its simple, useful, and affordable synthesis as well as its bared eye detection as well as high sensitivity and selectivity.

6 Conclusions

We describe an easy-to-use mono Schiff base colorimetric, turn-off fluorescent, sensitive and selective chemosensor **L** for the detection of Pb^{2+} in $CH_3OH–H_2O$ (1 : 1, v/v) with fluorometric detection limits of 9.9×10^{-7} M and colorimetric detection limits of 1.2×10^{-6} M. These values are significantly lower than the WHO-determined acceptable concentration in drinking water. DFT investigations, IR spectroscopy, NMR titration and ESI-mass spectrometry were used to examine the sensing mechanism of **L** towards Pb^{2+} ion. The potential of the chemosensor **L** has been demonstrated by its ability to detect Pb^{2+} ions in real samples, including biological materials such as BSA and building INHIBIT type of the molecular logic gate.

Data availability

The data are included in the ESI† of the manuscript.

Author contributions

Vanshika Sharma: conceptualization, methodology, visualization and writing – first draft. Srishti Dutta: investigation, formal analysis. Devanand Sahu: theoretical calculations. Sanchita Das: X-ray single crystal structure determination. Dr Goutam Kumar Patra: conceptualization, review, editing, funding acquisition and supervision.

Conflicts of interest

The authors declare no conflicts of interest.

Acknowledgements

G. K. P. would like to thank the Department of Science and Technology (SR/FST/CSI-264/2014 and EMR/2017/0001789) and Department of Biotechnology, Government of India, New Delhi for financial support.

References

1 M. Medfu Tarekegn, F. Zewdu Salilih and A. I. Ishetu, *Cogent Food Agric.*, 2020, **6**, 1783174.

2 J. M. Jacob, C. Karthik, R. G. Saratale, S. S. Kumar, D. Prabakar, K. Kadirvelu and A. Pugazhendhi, *J. Environ. Manage.*, 2018, **217**, 56–70.

3 A. Kumar, A. Kumar, C.-P. M. M. S., A. K. Chaturvedi, A. A. Shabnam, G. Subrahmanyam, R. Mondal, D. K. Gupta, S. K. Malyan, S. S. Kumar, S. A. Khan and K. K. Yadav, *Int. J. Environ. Res. Public Health*, 2020, **17**, 2179.

4 N. R. Jyothi, *Heavy Metals-Their Environmental Impacts and Mitigation*, 2020, pp. 1–12.

5 N. Rees and R. Fuller, *The Toxic Truth: Children's Exposure to Lead Pollution Undermines a Generation of Future Potential*, Unicef, 2020.

6 G. M. Hettiarachchi, A. R. Betts, W. G. Chandima Wekumbura, L. Lake, M. M. Mayer, K. G. Scheckel and N. T. Basta, *Evaluation of the Spreading Dynamics and Interactions of Lead-Carrier Microplastics Affected by Biofilm: A Mini-Review*, Elsevier, 2024, pp. 113–150.

7 S. B. Shah, *Heavy Metals in Scleractinian Corals*, 2021, pp. 1–26.

8 N. Burnase, S. Jaiswal and A. Barapatre, *Medical Geology in Mining: Health Hazards Due to Metal Toxicity*, 2022, pp. 127–186.

9 L. N. Kitui, Doctoral dissertation, JKUAT-IEET, 2022.

10 S. Dutta, B. Gorain, H. Choudhury, S. Roychoudhury and P. Sengupta, *Environ. Sci. Pollut. Res.*, 2022, **29**(41), 62067–62092.

11 M. S. Collin, S. K. Venkatraman, N. Vijayakumar, V. Kanimozhi, S. M. Arbaaz, R. G. S. Stacey, J. Anusha, R. Choudhary, V. Lvov, G. I. Tovar, F. Senatov, S. Koppala and S. Swamiappan, *J. Hazard. Mater. Adv.*, 2022, **7**, 100094.

12 O. Sarkar, K. K. Dey, S. Islam and A. Chattopadhyay, *Biomarkers Toxicol.*, 2022, 1–28.

13 J. Khatun, A. Intekhab and D. Dhak, *Toxicology*, 2022, **477**, 153274.

14 N. Munir, M. Jahangeer, A. Bouyahya, N. El Omari, R. Ghchime, A. Balahbib, S. Aboulaghras, Z. Mahmood, M. Akram, S. M. Ali Shah, I. N. Mikolaychik, M. Derkho, M. Rebezov, B. Venkidasamy, M. Thiruvengadam and M. A. Shariati, *Sustainability*, 2021, **14**, 161.

15 M. B. Virgolini and M. Aschner, *Advances in Neurotoxicology*, 2021, vol. 5, pp. 159–213.

16 J. G. Paithankar, S. Saini, S. Dwivedi, A. Sharma and D. K. Chowdhuri, *Chemosphere*, 2021, **262**, 128350.

17 S. Gudadhe, S. K. Singh and J. Ahsan, *Lead Toxicity Mitigation: Sustainable Nexus Approaches*, 2024, pp. 125–145.

18 S. Hemmaphan and N. K. Bordeerat, *Toxicol. Int.*, 2022, **29**(3), 321–328.

19 H. Liu, W. Zhang, L. Jin, S. Liu, L. Liang and Y. Wei, *Int. J. Mol. Sci.*, 2023, **24**, 6279.

20 J. Prathiksha, R. K. Narasimhamurthy, H. S. Dsouza and K. D. Mumbrekar, *Mol. Biol. Rep.*, 2023, **50**, 5465–5479.

21 P. Singh, P. Mitra, T. Goyal, S. Sharma and P. Sharma, *Biol. Trace Elem. Res.*, 2021, **199**, 1707–1714.

22 A. Kumar, A. Kumar, C.-P. M. M. S., A. K. Chaturvedi, A. A. Shabnam, G. Subrahmanyam, R. Mondal, D. K. Gupta, S. K. Malyan, S. S. Kumar, S. A. Khan and K. K. Yadav, *Int. J. Environ. Res. Public Health*, 2020, **17**, 2179.

23 V. I. Naranjo, M. Hendricks and K. S. Jones, *Pediatr. Neurol.*, 2020, **113**, 51–55.

24 S. Dasharathy, S. Arjunan, A. Maliyur Basavaraju, V. Murugasen, S. Ramachandran, R. Keshav and R. Murugan, *J. Evidence-Based Complementary Altern. Med.*, 2022, **1**, 1–11.

25 WHO, *WHO specifications and evaluations for public health pesticides: Bacillus thuringiensis subspecies israelensis strain AM65-52*, World Health Organization, Geneva, 2007, **http://www.who.int/whopes/quality/Bti_eval_spec_Jun_07.pdf**.

26 M. B. Rabinowitz, G. W. Wetherill and J. D. Kopple, *J. Clin. Invest.*, 1976, **58**, 260–270.

27 K. J. Rodriguez, A. Alva, V. T. Santos and A. Roman-Gonzalez, *Int. J. Adv. Comput. Sci. Appl.*, 2019, **10**(6), 496–499.

28 J. F. Flores-Aguilar, G. Islas, J. A. Rodríguez, M. E. Paez-Hernandez, C. A. Galan-Vidal and I. S. Ibarra, *J. Mex. Chem. Soc.*, 2022, **66**, 8747–8754.

29 A. Ghosh and G. Das, *New J. Chem.*, 2021, **45**, 8747–8754.

30 N. Laur, R. Kinscherf, K. Pomytkin, L. Kaiser, O. Knes and H.-P. Deigner, *PLoS One*, 2020, **15**, e0233357.

31 C. E. Rahm, P. Gupta, V. K. Gupta, A. Huseinov, B. Griesmer and N. T. Alvarez, *Analyst*, 2022, **147**, 3542–3557.

32 N. H. Pratiwi, M. Y. Azis, D. A. Setyorini and R. S. Rahayu, *Anal. Bioanal. Electrochem.*, 2022, 331–347.

33 Z. Chen, Z. Zhang, J. Qi, J. You, J. Ma and L. Chen, *J. Hazard. Mater.*, 2023, **441**, 129889.

34 M. Sengan, R. K. Kamlekar and A. Veerappan, *Spectrochim. Acta, Part A*, 2020, **239**, 118485.

35 B. P. Sharma, J. Adhikari Subin, B. P. Marasini, R. Adhikari, S. K. Pandey and M. L. Sharma, *Heliyon*, 2023, **9**(4), e15239.

36 R. Meena, P. Meena, A. Kumari, N. Sharma and N. Fahmi, *Schiff Base in Organic, Inorganic and Physical Chemistry*, 2023.

37 M. K. Goshisht, G. K. Patra and N. Tripathi, *Mater. Adv.*, 2022, **3**, 2612–2669.

38 Ekta, D. Utreja and S. Sharma, *ChemistrySelect*, 2023, **8**, e202204038.

39 R. V. Rathod, D. Mondal and S. Bera, *Anal. Bioanal. Chem.*, 2020, **412**, 3177–3186.

40 M. Li, Y. Gao, Y. Zhang, S. Gong, X. Tian, Y. Yang, X. Xu, Z. Wang and S. Wang, *Spectrochim. Acta, Part A*, 2021, **262**, 120135.

41 A. Ghorai, J. Mondal and G. K. Patra, *New J. Chem.*, 2016, **40**, 7821–7830.

42 I. Okada, T. Fukuda, Y. Kuroda, K. Noguchi, K. Chiba and Y. Kitano, *Synthesis*, 2017, **49**, 1301.

43 H. Khanmohammadi and A. Abdollahi, *Dyes Pigm.*, 2012, **94**, 163.

44 M. J. MacLachlan, M. K. Park and L. K. Thompson, *Inorg. Chem.*, 1996, **35**, 5492.

45 N. Zare, A. Zabardasti, M. Dusek and V. Eigner, *J. Mol. Struct.*, 2018, **1163**, 388.

46 D. Sarkar, A. Pramanik, S. Jana, P. Karmakar and T. K. Mondal, *Sens. Actuators, B*, 2015, **209**, 138–146.

47 Y. Ma, F. Wang, S. Kambam and X. Chen, *Sens. Actuators, B*, 2013, **188**, 1116–1122.

48 Z. Dong, X. Le, P. Zhou, C. Dong and J. Ma, *RSC Adv.*, 2014, **4**, 18270–18277.

49 G. K. Patra, R. Chandra, A. Ghorai and K. K. Shrivas, *Inorg. Chim. Acta*, 2017, **462**, 315–322.

50 A. K. Manna, J. Mondal, R. Chandra, K. Rout and G. K. Patra, *Anal. Methods*, 2018, **10**, 2317–2326.

51 A. K. Manna, M. Sahu, K. Rout, U. K. Das and G. K. Patra, *Microchem. J.*, 2020, **157**, 104860.

52 V. Sharma, B. Sahu, U. K. Das and G. K. Patra, *Inorg. Chim. Acta*, 2023, **552**, 121491.

53 *SMART & SAINT Software Reference Manuals*, version 5.0, Bruker AXS Inc., Madison,WI, n.d,.

54 T. Gruene, H. W. Hahn, A. V. Luebben, F. Meilleur and G. M. Sheldrick, *J. Appl. Crystallogr.*, 2014, **47**, 462–466.

55 L. J. Farrugia, *J. Appl. Crystallogr.*, 1999, **32**, 837–838.

56 S. S. Bozkurt, S. Ayata and I. Kaynak, *Spectrochim. Acta, Part A*, 2009, **72**(4), 880–883.

57 N. George, G. Singh, R. Singh, G. Singh, Priyanka, H. Singh, G. Kaur and J. Singh, *J. Mol. Struct.*, 2023, **1288**, 135666.

58 V. Sharma, S. Savita and G. K. Patra, *RSC Adv.*, 2024, **14**, 3289–3303.

59 K. Rout, A. K. Manna, M. Sahu, J. Mondal, S. K. Singh and G. K. Patra, *RSC Adv.*, 2019, **9**, 25919–25931.

60 V. Sharma, S. Savita and G. K. Patra, *RSC Adv.*, 2024, **14**, 3289–3303.

61 M. Chandra, K. Sharma and S. Chandra, *Anal. Bioanal. Electrochem.*, 2022, **14**(9), 860–870.

62 S. Sowmiyha, V. V. Kumar, J. Pitchaimani, V. Madhu, R. Thiagarajan, N. S. Subramanian and S. P. Anthony, *J. Lumin.*, 2018, **203**, 42–49.

63 G. Prabakaran, R. Vickram, K. Velmurugan, C. Immanuel David, S. Prince Makarios Paul, R. Suresh Kumar, A. I. Almansour, K. Perumal, A. Abiram, J. Prabhu and R. Nandhakumar, *Food Chem.*, 2022, **395**, 133617.

64 J. Zhao, C. Li, S. Wei, C. Lü and L.-W. Zou, *Spectrochim. Acta, Part A*, 2023, **300**, 122904.